**Title:** Optimizing aerial imagery collection and processing parameters for drone-based individual tree mapping in structurally complex conifer forests

**Authors:**

Derek J. N. Young; Department of Plant Sciences, University of California, Davis; djyoung@ucdavis.edu

Michael J. Koontz; Earth Lab, University of Colorado, Boulder; mikoontz@gmail.com

JonahMaria Weeks; Department of Environmental Science and Policy, University of California, Davis; jsweeks@ucdavis.edu

**Abstract:**

Recent advances in remotely piloted aerial system ("drone") and imagery processing technologies have enabled individual tree mapping in forest stands across broad areas with low-cost equipment and minimal ground-based data collection. One such method, "structure from motion" (SfM), involves collecting many partially overlapping aerial photos over a focal area and using photogrammetric analysis to infer 3D structure and detect individual trees. SfM-based forest mapping involves myriad decisions surrounding the selection of methods and parameters for imagery acquisition and processing, but no studies have comprehensively and quantitatively evaluated the influence of these parameters on the accuracy of the resulting tree maps.

We collected and processed drone imagery of a moderate-density, structurally complex mixed-conifer stand. We tested 22 imagery collection methods (altering flight altitude, camera pitch, and image overlap), 12 imagery processing parameterizations, and 286 tree detection methods (algorithms and their parameterizations) to create 7,568 tree maps. We compared these maps to a 3.23-ha ground-truth map of 1,916 trees > 5 m tall that we created using traditional field survey methods.

We found that the accuracy of individual tree detection (ITD) and the resulting tree maps was generally maximized by collecting imagery at high altitude (120 m) with at least 90% image-to-image overlap, photogrammetrically processing images into a canopy height model (CHM) with a 2-fold upscaling (coarsening) step, and detecting trees from the CHM using a variable window filter after first applying a moving-window mean smooth to the CHM. Using this combination of methods, we mapped trees with an accuracy that exceeds expectations for our structurally complex forest based on other recent results (for overstory trees > 10 m tall, sensitivity = 0.69 and precision = 0.90). Remotely-measured tree heights corresponded to ground-measured heights with $R^2 = 0.95$. Accuracy was higher for taller trees and lower for understory trees, and it is likely to be higher in lower density and less structurally-complex stands.

Our results may guide others wishing to efficiently produce individual-tree maps of conifer forests over broad extents without investing substantial time tailoring imagery acquisition and processing parameters. The resulting tree maps create opportunities for addressing previously intractable ecological questions and increasing the efficiency of forest management.

## Introduction

Forest inventories are critical resources for developing and testing ecological theories (Bazzaz, 1975; Hubbell et al., 1999; Lasky et al., 2014; Whittaker, 1956; Wright et al., 2010) and informing forest management (Ager et al., 2021; Dixon, 2002; North et al., 2021; Young et al., 2020). Forest inventories and tree maps have traditionally been completed by ground-based field crews and require substantial time, labor, and financial investment (Gray et al., 2012; USDA Forest Service, 2016); as a consequence, they are limited in the area they can cover. To address these constraints, forest mapping approaches have more recently begun to rely on remote sensing data to enable creation of continuous forest maps over broad areas. Remote sensing-based forest mapping has traditionally taken an "area-based approach" in which remote sensing data (e.g., spectral data from satellite or aerial imagery) are used to estimate forest summary statistics such as tree density, mean tree height, and aboveground biomass (De Luca et al., 2019; Jayathunga et al., 2018; Puliti et al., 2019; Rodman et al., 2019). The increasing prevalence of higher resolution remote sensing data has recently enabled a more direct approach to forest mapping that involves detecting and characterizing individual trees (Jeronimo et al., 2018; Koontz et al., 2021; Swayze et al., 2021).

Small remotely piloted aerial systems (RPAS, or "drones") provide data at a scale particularly well suited for individual tree detection (ITD). A fundamental technique in drone-based forest mapping involves collecting many partially overlapping images in a dense grid over the study area (Dandois & Ellis, 2013; Westoby et al., 2012). The images are supplied to a photogrammetry algorithm, which employs principles of perspective and triangulation to estimate the 3D structure of the landscape by quantifying the amount by which landscape features move relative to each other between images. This method is commonly referred to as "structure from motion" (SfM; Dandois & Ellis, 2013; Westoby et al., 2012) because the many optical perspectives from the drone as it moves allows modeling of the 3D structure of objects and landscapes. The structure data can be represented as a point cloud in which each point identifies a surface (e.g., leaf, stem, ground) that appears in multiple photos. The point cloud data can be processed into raster-format vegetation canopy height models (CHMs) (Fig. 1). SfM-derived point cloud data share many characteristics with aerial light detection and ranging (LiDAR) or aerial laser scanning (ALS) data, which can also be used for ITD (Jeronimo et al., 2018; Zaforemska et al., 2019). A major difference is that SfM-derived point clouds are usually substantially denser and higher resolution (e.g., > 100 points $m^{-2}$, this study) than LiDAR-derived point clouds (often < 8 points $m^{-2}$; USGS, 2018; Weinstein et al., 2021). Drone-based data is also much less costly to obtain and can be collected from specific focal areas with high frequency and little advance planning (Camarretta et al., 2020; Mlambo et al., 2017). However, relative to SfM data, airborne LiDAR data usually have larger footprints and may better capture sub-canopy structure because some laser pulses penetrate the canopy (Jayathunga et al., 2018; Lisein et al., 2013).

Numerous algorithms have been developed to detect individual trees from CHMs, usually based on a moving window local maximum search (Popescu & Wynne, 2004), and directly from point clouds (Li et al., 2012; Xiao et al., 2019). ITD accuracy varies considerably depending on the stand structural characteristics and algorithms used, with higher accuracy in lower-density stands and in overstory vs. understory trees. ITD accuracy is arguably best summarized using the F-score, the harmonic mean of the sensitivity (proportion of field trees detected) and the precision (proportion of detected trees that match field trees) and which ranges between 0 (no field trees detected) and 1 (all field trees detected and no false positive detections). Recent ITD work using drone-derived SfM products for overstory trees (Creasy et al., 2021; Mohan et al., 2017) or for all trees in low- to moderate-density stands (Belmonte et al., 2020; Bonnet et al., 2017; Swayze et al., 2021) has obtained F scores ranging roughly between 0.75 and 0.85, whereas for higher-density stands or understory trees, performance tends to be lower (e.g., F < 0.65; Creasy et al., 2021). In a hybrid ITD--area-based approach, Koontz et al. (2021) used SfM data to quantify tree density across multiple structurally complex and relatively dense (mean tree density > 450 trees ha$^{-1}$) yellow pine/mixed-conifer stands (Safford & Stevens, 2017) in the Sierra Nevada of California with $R^2 = 0.45$. The height and canopy extent of automatically detected trees can usually be measured from CHM or point cloud data with high accuracy (RMSE: 3-7% and $R^2 > 0.70$; Belmonte et al., 2020; Creasy et al., 2021; Silva et al., 2016).

Despite the promise of drone-based tree mapping using SfM, relatively little work has quantitatively evaluated the influence of different imagery collection, imagery processing, and tree detection methods on the accuracy of the resulting tree maps. Using an oblique (as opposed to directly downward, or “nadir”) camera pitch can increase the accuracy of digital terrain models derived from drone images in areas with low vegetation cover (Nesbit & Hugenholtz, 2019) and in forests can increase the point cloud density in the understory (Díaz et al., 2020), but the only published evaluation of camera pitch specifically in the context of individual tree detection (ITD) found that tree detection accuracy was greater with a nadir vs. oblique camera pitch (Swayze et al., 2021). No study to date has directly evaluated the potential for combining nadir and oblique imagery to improve ITD accuracy. Flight (image collection) altitude may additionally affect 3D reconstruction quality, though previous work has found little difference in ITD performance among flights conducted between 64 and 115 m above ground level (Swayze et al., 2021) and between 50 and 100 m above ground level (Torres-Sánchez et al., 2018). Finally, while increased image collection density (i.e., overlap) is associated with increased point cloud quality and density (Dandois & Ellis, 2013; Frey et al., 2018; Ni et al., 2018), it also increases image dataset size and acquisition and processing times. Increasing image overlap can increase ITD accuracy (Swayze et al., 2021), with diminishing returns to accuracy at increasingly high overlap (Torres-Sánchez et al., 2018).

Once imagery is collected, the analyst has numerous choices of parameters to use for subsequent photogrammetric processing to generate point clouds and canopy height models, including the image resolution to use for the image alignment and point cloud creation and the extent to which potential outliers should be filtered from the point cloud. Using full image resolution during processing may increase point cloud detail and density (Jayathunga et al., 2018; Lisein et al., 2013), but (a) higher resolution data can substantially increase processing times, (b) high-resolution images may be difficult to align and compare when they include small surfaces like leaves and branches that move or blow in the wind, and (c) the extent to which any increase in point cloud detail translates to improved ITD performance is not well known. Only one study to our knowledge has evaluated image resolution and point cloud filtering parameters in the context of ITD (Tinkham & Swayze, 2021). Using the Metashape v1.6.4 photogrammetry software (Agisoft, LLC), it found that retaining maximal image resolution and minimizing outlier filtering during point cloud generation yielded the greatest ITD performance. It did not evaluate the influence of image resolution during the alignment stage.

Finally, once photogrammetric products are generated, there are myriad options for ITD algorithm selection and parameterization. Several studies have compared the accuracy of different ITD algorithms and/or parameterizations applied to SfM-derived canopy height models and point clouds. Mohan et al. (2017) tested 4 different parameterizations of a CHM-based fixed window filter, combined factorially with 4 different CHM smoothing intensities, for a total of 16 parameter sets. Creasy et al. (2021) evaluated 97 different parameterizations of a CHM-based variable- and fixed- window filtering method (Plowright, 2021). Shin et al. (2018) tested 16 parameterizations of a point cloud-based ITD algorithm (Li et al., 2012). Koontz et al. (2021) tested a total of 177 parameter sets across 7 different CHM- and point cloud-based ITD algorithms, identifying a parameterization of a point cloud-based method (Li et al., 2012) as the most accurate. While it also included a test of a variable window filtering algorithm (Plowright, 2021), it tested only 3 parameter sets for this algorithm and thus provides limited opportunity for comparison with previous studies that employed this method.

Quantitative evaluations of SfM-based ITD methods to date have generally evaluated only imagery collection parameters, only imagery processing parameters, or only tree detection algorithms. However, evaluating the influence of these categories of variables jointly may allow detection of consistent effects vs. idiosyncrasies and may reveal important interactions that enable meaningful improvements in ITD accuracy and efficiency. In addition, many evaluations of ITD methods have been conducted in stands that are structurally relatively simple and of relatively low tree density, potentially yielding parameter selection and tree detection performance different than may be expected in higher-density, more structurally-complex stands. In the present study, we evaluate multiple factorial combinations of imagery collection parameters (flight altitude, camera pitch, and image overlap), imagery processing parameters (image resolution for image alignment and for dense cloud generation, and point cloud outlier filtering intensity), and tree detection methods (algorithm and parameterization), for a total of 7,568 combinations, in a moderately dense, structurally complex mixed-conifer stand in the Sierra Nevada of California.

## Methods

### *Overview*

We created a ground-truth tree map of 1,916 trees > 5 m tall in a 3.23-ha focal area using traditional survey methods. We also used automated algorithms to create 7,568 tree maps from aerial imagery collected by drone to evaluate the influence of image acquisition and processing parameters on aerial tree mapping accuracy. In Stage 1, we identified the best-performing photogrammetry processing processing parameters and automated tree detection methods. In Stage 2, we applied those methods to identify the best image acquisition parameters (e.g., flight altitude, camera pitch, and image overlap) (Table 1).

**Table 1:** The combination of photo set parameters, photogrammetry parameters, and tree detection methods tested. Within each row, all factorial combinations of the listed photo set parameters, photogrammetry parameters, and tree detection methods were tested.

| **Comparison stage** | **Photo set parameters tested (Table 2)** | **Photogrammetry parameters tested (Table 3)** | **Tree detection methods tested (Supplemental Data S1 and S2)** | **Total resulting tree maps evaluated** |
|---|---|---|---|---|
| Stage 1 (Identify best photogrammetry and tree detection parameters) | High nadir 90/90, Low nadir 90/90 | Parameter sets 7-18 | VWF methods 1-228, Point cloud methods 1-58 | 6,864 |
| Stage 2 (Identify best flight and image overlap parameters) | All 22 listed in Table 2 | Parameter sets 9, 11, 15, 16 | VWF methods 109, 110, 113, 120, 121, 122, 185, 196 | 704 |

*Focal area*

Our study site was a 3.23 ha mixed-conifer forest (Safford & Stevens, 2017) stand in Emerald Bay State Park on the shore of Lake Tahoe in the Sierra Nevada of California (Fig. 1a). The stand is co-dominated, in decreasing order of abundance, by ponderosa pine (*Pinus ponderosa*), incense cedar (*Calocedrus decurrens*), Jeffrey pine (*Pinus jeffreyi*), and white fir (*Abies concolor*). The stand has high structural complexity, with a continuous size distribution and small trees interspersed with larger trees and often underneath their canopies (Fig. 1b).

A ground-truth stand inventory (see *Ground-based tree mapping*) revealed that the 3.23-ha focal area contained a total of 2135 trees with DBH > 7.5 cm (661 trees ha$^{-1}$), 1916 trees with DBH > 10 cm (593 trees ha$^{-1}$), 1780 trees with height > 5 m and DBH > 7.5 cm (551 trees ha$^{-1}$), and 1100 trees with height > 10 m and DBH > 7.5 cm (341 trees ha$^{-1}$). Of all trees with DBH > 7.5 cm, 292 (14%) were dead (and still standing, but potentially partially broken).

*Ground-based tree mapping*

We developed a 3.23 ha ground-truth tree map against which to evaluate our drone-based maps. To construct the map, we established a grid of “primary centerpoints” with approximately 25 m spacing across the focal area. From each primary centerpoint, we measured the horizontal distance (using a laser rangefinder/hypsometer) and azimuth (using a sighting compass) to each nearby tree with diameter at breast height (DBH) > 7.5 cm. We marked trees with chalk to avoid recording the same tree from multiple centeroints and to ensure a complete survey. If one or more trees were not visible from a primary centerpoint, we established a secondary centerpoint, referenced using distance and azimuth from the nearest primary centerpoint, from which to measure the additional trees. We measured the height of each tree using a laser hypsometer/rangefinder. We recorded the geographic coordinates of each primary centerpoint using a 216-channel L1/L2 GNSS receiver (TRIUMPH-2, Javad

GNSS, Inc.). We then computed the cartesian geographic coordinates (in the California Albers projection) of each tree (and secondary centerpoint) based on its distance and azimuth from its respective centerpoint using trigonometric functions.

The primary centerpoint coordinates measured by GNSS included some error due to tree canopy cover and normal atmospheric distortion of GNSS signals. To correct for this error, we used a preliminary drone-based stem map (see section *Individual tree detection (ITD)*) as a reference and manually shifted the locations of each primary centerpoint (and thus all trees measured relative to that centerpoint) to improve the alignment of prominent ground-measured trees with their clearly apparent counterparts in the drone-derived map. The intended boundaries of the ground-based tree map were unclear in some areas, and some primary centerpoints along the edge could not be confidently aligned because there were few prominent trees, so we adjusted the boundary of the focal area inward from the originally planned 4-ha square to obtain a 3.23-ha focal area within which we were confident that almost all trees with DBH > 7.5 cm were accurately mapped.

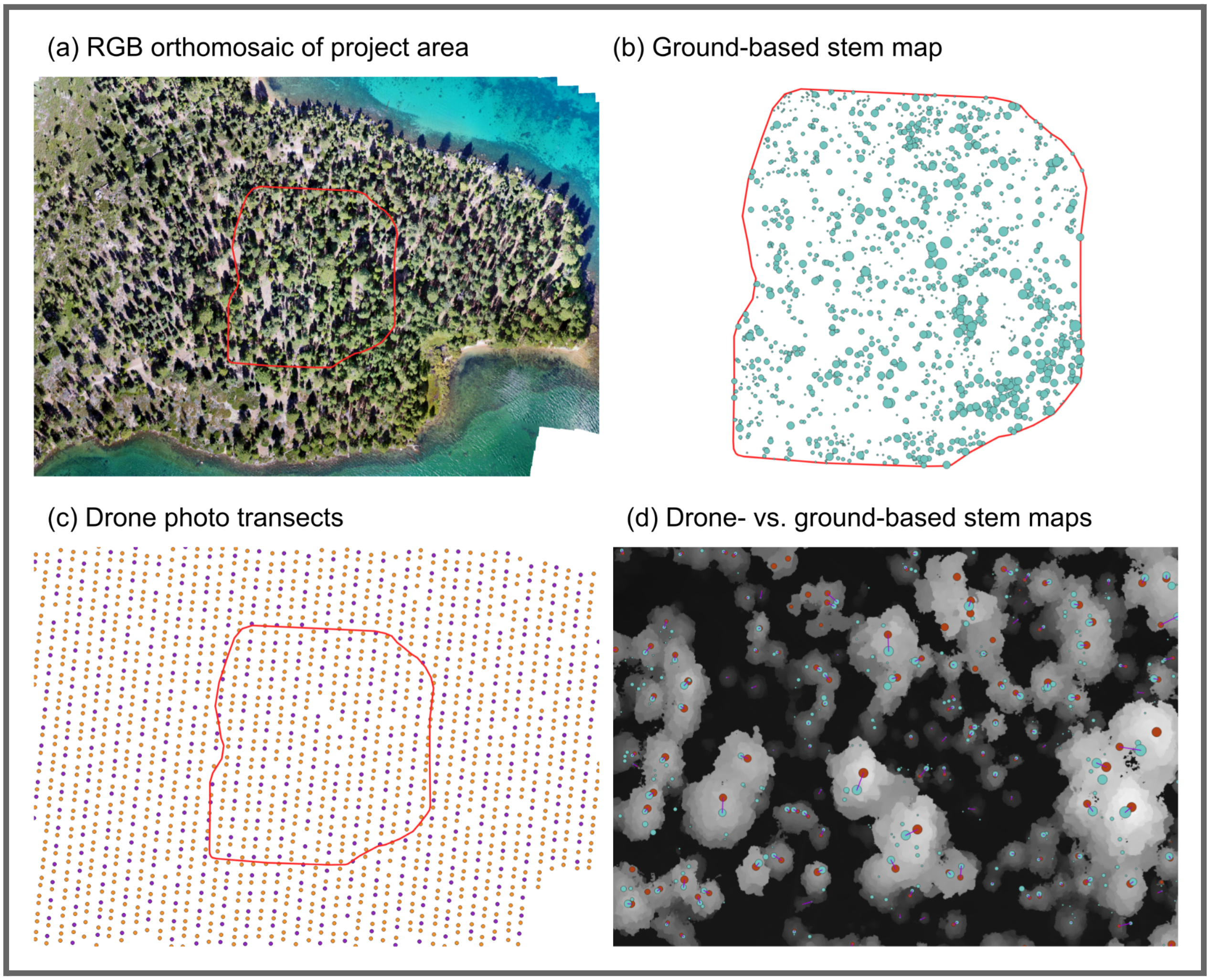

**Fig. 1:** (a) RGB orthomosaic of the project vicinity, with the 3.23-ha focal area indicated with a red outline. (b) The ground-based tree stem map of all trees > 5 m tall constructed as a basis for evaluation of drone-derived stem maps, with larger points indicating taller trees. (c) Spatial

locations of drone photos from two drone photo sets (Table 3) ("high nadir" 95% front and side overlap in yellow; and "high nadir" 90% front and side overlap in purple). (d) Canopy height model (lighter indicates taller) of a section of the focal area, with ground-mapped trees shown as light blue points, drone-mapped trees shown as dark red points, and pairings between ground- and drone-mapped trees shown as purple lines. In (d), the canopy height model was created by applying photogrammetry parameter set 16 (Table 4) to the "high nadir" photo set with 90% front and side overlap (Table 3). The drone-derived stem map was obtained by applying tree detection algorithm "vwf_059" (Supplemental data S1) to this same canopy height model.

### *Imagery collection and pre-processing*

We collected RGB (red, green, blue) aerial photographs using a DJI Phantom 4 Advanced quadcopter (SZ DJI Technology Co., Ltd.), which has a 1", 20 megapixel (5472 x 3648 pixel) CMOS sensor, an 8.8 mm focal length, and an 84° field of view. We planned and executed missions using the MapPilot software (Drones Made Easy) on an iPad Pro 9.3" (Apple Inc.) connected to the drone's remote controller. The missions consisted of multiple parallel straight-line transects across the study area (and extending at least 100 m beyond it on all sides) (Fig. 1c), with transect spacing and image spacing along transects set to achieve the specified percentage of overlap between adjacent images (Table 3). Actual image overlap inevitably differs slightly from the specified overlap (e.g., due to occasionally missed photos, a normal occurrence with some common DJI drones; Fig. 1c), so we refer to the overlap amount as the "nominal overlap," reflecting what a future user may expect when using these settings with a similar aircraft. We collected multiple image datasets using different flight parameters (altitude, gimbal pitch, and image overlap) (Table 2). For the missions with 25° camera gimbal pitch (i.e., "oblique", with camera angled 25° up from nadir), we flew two perpendicular sets of transects (N-S and E-W) so that a given point on the landscape would be photographed from four directions as opposed to only two. For the nadir missions, the transect orientation was irrelevant because all images were taken directly top-down and we therefore only flew N-S transects.

All missions used automatic exposure and automatic white balance settings and were flown in MapPilot's "connectionless" mode. We used the "terrain awareness" function so that the aircraft remained at a constant altitude above ground level throughout the mission. Images were collected between 11 am and 3 pm local time (where solar noon was c. 1:04 pm) on 9-12 September, 2019. During the flights, winds were light to moderate, visibility was high, and conditions were mostly clear with rare small clouds for brief periods.

To test the effect of image overlap on the quality of the resulting tree maps, we subsetted the photo sets to effectively reduce image overlap by retaining every *n*th image on every *n*th transect. For example, for the missions with 0° gimbal pitch and originally 95% front and side overlap, we retained every second image on every second transect to achieve a nominal 90% front and side overlap, and we retained every 4th image on every 4th transect to achieve a nominal 80% front and side overlap (Fig. 1c). We repeated this process to obtain multiple factorial combinations of nominal front and side overlaps. This thinning approach follows that used by previous studies (Frey et al., 2018; Torres-Sánchez et al., 2018) except that we performed side thinning in addition to forward thinning. In thinning the 25° camera pitch missions, we considered each out-and-back segment (e.g., north-facing and subsequent south-facing sequence of photos) to be a single “round-trip transect” and selected every 2nd or 4th round-trip transect. We did this to avoid obtaining a photo set with cameras facing in only a single direction (e.g., only N-facing, as would occur when selecting every other transect of a N-S transect flight).

**Table 2:** Parameters for image collection flights.

| Photo set (mission) name | Altitude above ground (m) | Camera gimbal pitch | Transect orientation | Forward overlap (%) | Side overlap (%) |
|---|---|---|---|---|---|
| High nadir (14) | 120 | 0° (nadir) | N-S | 95 | 95 |
| Low nadir (15) | 90 | 0° (nadir) | N-S | 95 | 95 |
| High oblique (26) | 120 | 25° (oblique) | N-S | 90 | 90 |
| | | | E-W | 90 | 90 |
| Low oblique (27) | 90 | 25° (oblique) | N-S | 90 | 90 |
| | | | E-W | 90 | 90 |

Prior to photogrammetric processing of the image sets, we combined the photos from N-S and E-W flights of the same mission (e.g., the 120 m altitude, 25° gimbal pitch mission). Combining the photos from two 90%/90% front/side overlap flights (i.e., two transect orientations) resulted in a photo set with twice the image density relative to a mission with single-orientation transects (i.e., N-S only) with 90%/90% front/side overlap. We consider these photo sets to have a nominal 92.5% front and side overlap (equivalent image density as a 95%/90% front/side overlap mission or a 90%/95% front/side overlap mission, but without explicitly different front vs. side overlaps). Similarly, combining the photos from two 80%/80% front/side overlap transect orientations resulted in a mission with a nominal 85%/85% front/side overlap.

Finally, we tested whether combining nadir (0°) and oblique (25°) camera pitch missions into a single composite photo set yielded improved photogrammetric performance and ultimately more accurate tree maps. For each flight elevation (90 m and 120 m), we prepared two composite photo sets. First, we combined the 90%/80% front/side overlap nadir photo set with the 85%/85% front/side overlap oblique photo set of the same elevation to obtain a nominal 90%/90% overlap composite photo set (with photo density equivalent to that of a single 90%/90% overlap mission). Second, we combined the 95%/90% front/side overlap nadir photo set with the 92.5%/92.5% oblique photo set to obtain a nominal 95%/95% overlap composite photo set (with equivalent photo density as a single 95%/95% overlap mission). The resultant photo sets are listed in Table 3.

**Table 3:** The photo set (flight and image overlap) parameters tested to evaluate the effect of flight altitude, camera pitch, and image overlap on quality of the resulting photogrammetry products for tree mapping (Stage 2). The multiple image overlap values were obtained by thinning the originally collected image datasets (Table 2). The bolded text indicates the two photo sets that were also used in identifying the best Metashape photogrammetry parameter sets (Stage 1).

| Photo set group | Altitude above ground (m) | Camera gimbal pitch | Nominal image overlaps tested (front/side) (%) |
|---|---|---|---|
| High nadir | 120 | 0° | 80/80, 90/80, 80/90, **90/90**, 95/90, 90/95, 95/95 |
| Low nadir | 90 | 0° | 80/80, 90/80, 80/90, **90/90**, 95/90, 90/95, 95/95 |
| High oblique | 120 | 25° | 85/85, 92.5/92.5 |
| Low oblique | 90 | 25° | 85/85, 92.5/92.5 |
| High composite | 120 | 0° and 25° | 90/90, 95/95 |
| Low composite | 90 | 0° and 25° | 90/90, 95/95 |

### *Ground control points*

To minimize horizontal and vertical errors in digital surface models and 3D point clouds produced through photogrammetric processing of drone images, it is common practice to use ground control points (GCPs) (James & Robson, 2014). Generally, GCPs are targets that are placed in the project area and visible in the drone imagery. Their positions are measured using a differentially-corrected GPS or surveyor's total station and used to inform and constrain the locations of the images during photogrammetric matching and alignment. To reduce the field time required, we did not place GCPs but instead used existing natural features as GCPs. For each of the imagery missions (Table 2), we identified 8 to 9 features at ground level (e.g., crossed logs or a prominent corner of a large rock at ground level) that were visible in both the drone imagery and in Google Earth imagery. We used the geospatial coordinates of the features in the Google Earth imagery as their "true" horizontal locations and extracted their "true" elevations from a 10 m USGS digital elevation model (USGS, 2018) using bilinear interpolation. We examined Google Earth imagery in QGIS v3.12 using the Google XYZ web tile service. We then identified each of these features in 6 to 8 drone photos and recorded their pixel coordinates. For this last step, we used only photos from the most heavily thinned version of the photo set so that the same images would be present in all of the thinned photo sets derived from the mission (since the most thinned set--e.g., 80% front and side overlap--is a subset of the less heavily thinned sets--e.g., 90% and 95% overlaps).

### *Photogrammetric processing*

We performed photogrammetric structure-from-motion (SfM) processing of the aerial image sets (see *Introduction*) to produce 3D point clouds and digital surface models using

Metashape version 1.6.5 (Agisoft, LLC). We interfaced with Metashape via its Python API using the UC Davis Metashape workflow software version 0.1.0 (Young et al., 2021), which executes a full photogrammetry workflow from end to end, using the processing parameters specified in a configuration file by the user, with a single command-line call. The workflow reads GCP location data from delimited text files prepared in advance (see *Ground control points*).

Our first objective was to determine the combination of photogrammetry processing parameters that maximized the quality of the photogrammetric products for the purpose of tree mapping (Stage 1). We evaluated all factorial combinations of the photo alignment quality parameter (low, medium, or high, corresponding to image upscaling factors of 4, 2, or 1, respectively), the dense cloud quality parameter (medium or high, corresponding to image upscaling factors of 4 or 2, respectively), and the depth filtering intensity parameter (mild or moderate). Upscaling factors refer to the amount by which the image resolution was upscaled (coarsened) in each dimension; for example, with an upscaling factor of 4, the resulting image resolution in x and y dimensions would be ¼ of its original, with each coarse pixel representing the average of 16 original pixels (a 4 x 4 square) (Agisoft, 2020). The three-way factorial combination of photo alignment quality, dense cloud quality, and depth filtering parameters yielded 12 different processing configurations, which we ran on two different aerial photo sets: the 120 m nadir (0° camera pitch) mission with 90% front and side photo overlap, and the 90 m nadir mission with 90% front and side photo overlap.

After identifying four Metashape parameter sets that yielded the best tree detection results for these two photo sets (see *Individual tree detection* and *Identification of best-performing methods*, below), we used each of these four parameter sets to process all of the photo sets (Table 3) to enable an evaluation of the effect of of flight altitude, image overlap, and camera pitch on tree mapping performance (Stage 2). Processing all 22 photo sets with the four Metashape parameter sets resulted in running 88 photogrammetry workflows. All processing parameters besides photo alignment quality, dense cloud quality, and depth filtering intensity were held constant across all runs. These included 100 maximum neighbors for dense cloud reconstruction, adaptive camera model fitting of all camera model parameters, and default Metashape Python API values for all other parameters. The workflow included a modified, automated version of a sparse point cloud filtering procedure recommended by the USGS (2017). Specifically, it involved removing the worst 20th percentile of points by reconstruction uncertainty (or all points with reconstruction uncertainty > 15, whichever removed less), removing the worst 30th percentile of points by projection accuracy (or all points with projection accuracy < 2, whichever removed less), and removing the worst 5th percentile of points by reprojection error (or all points with reprojection error > 0.3, whichever removed less). After then adding GCPs and optimizing cameras, the filtering procedure called for repeating the filtering based on reprojection accuracy using the same thresholds as previously.

In full, the Metashape workflow had the following steps: add photos, align photos, filter sparse cloud points, add GCPs, optimize cameras (using GCPs only), filter sparse cloud points again (by reprojection accuracy only), build dense cloud, and build digital surface model. The code we used to automate this workflow is published (Young et al., 2021).

**Table 4:** Metashape photogrammetry processing parameter combinations tested (Stage 1). The image upscaling factor (in parentheses) refers to the factor by which image resolution was upscaled (coarsened), in each dimension, prior to processing (photo alignment or dense cloud creation). The four parameter sets that yielded the best tree detection results and were subsequently used in the evaluations of flight altitude, camera pitch, and overlap (Stage 2) are bolded.

| Photogrammetry parameter set ID | Photo alignment quality (image upscaling factor) | Dense cloud quality (image upscaling factor) | Depth filtering intensity |
|---|---|---|---|
| 7 | low (4) | medium (4) | mild |
| 8 | low (4) | medium (4) | moderate |
| **9** | low (4) | high (2) | mild |
| 10 | low (4) | high (2) | moderate |
| **11** | medium (2) | medium (4) | mild |
| 12 | medium (2) | medium (4) | moderate |
| 13 | medium (2) | high (2) | mild |
| 14 | medium (2) | high (2) | moderate |
| **15** | high (1) | medium (4) | mild |
| **16** | high (1) | medium (4) | moderate |
| 17 | high (1) | high (2) | mild |
| 18 | high (1) | high (2) | moderate |

### *Post-processing of photogrammetry products*

The photogrammetry workflow was configured to produce a digital surface model (DSM), a continuous geospatial raster with the value of each cell representing the height (above sea level) of the highest surface detected at each x,y grid cell. Metashape's DSM raster output spatial resolution, which is linked to the ground sampling distance of the aerial photos (and ultimately to the flight altitude), was 0.066 m for the 120 m flights and 0.046 m for the 90 m flights. To process this DSM into a canopy height model (CHM), we used a 10-m resolution USGS digital elevation model (DEM) (USGS, 2018), which we interpolated to the resolution of the DSM using bilinear interpolation and then subtracted from the DSM (thus "normalizing" the DSM by removing the underlying topography, converting the elevations to "height above ground"). We then resampled the resulting CHM to a spatial resolution of 0.12 m because (a) this allowed us to compare CHMs derived from different flight altitudes (with different resolutions initially) and (b) in preliminary testing, this resolution resulted in slightly better tree detection performance than the original 0.046 - 0.066 m resolution (data not shown), potentially because it smooths over reconstruction artifacts.

The photogrammetry workflow also produced a 3D point cloud with a point density of roughly 100-500 points $m^{-2}$ (depending on the dense cloud quality setting). This point density was far greater than necessary to achieve maximal tree detection performance (data not shown) and resulted in unnecessarily large file sizes and processing times for the tree detection algorithms. For this reason, and to produce point clouds of similar density regardless of the photogrammetry settings, we thinned ("decimated") the point cloud to a nominal 50 points $m^{-2}$ using an algorithm that aims to yield a uniform point density across space. In practice, this algorithm reduced point density to between 70 and 100 points $m^{-2}$. As with the DSM, the elevations of points were initially relative to sea level. To normalize the point cloud and convert the point elevations to "height above ground", we used the same USGS DEM, which we interpolated to 0.05 m resolution using bilinear interpolation. We then subtracted from each point's elevation the elevation of the DEM grid cell above which the point was located. We performed all point cloud post-processing in R version 3.6.3 (R Core Team, 2020) using package lidR version 3.0.4 (Roussel, 2021a).

### *Individual tree detection (ITD)*

During Stage 1 of methods evaluation (focused on identifying the best Metashape photogrammetry parameters and tree detection algorithms), we tested a wide range of tree detection algorithms. We first tested the "variable window filter" (VWF) algorithm of Popesu and Wynne (2004) as implemented in the R package ForestTools version 0.2.1 (Plowright, 2021). This function uses the CHM raster and evaluates each pixel as a potential tree top by searching all pixels within a particular radius around the focal pixel and labeling the focal pixel as a tree top if it has the maximum height value with the search radius. The search radius is determined by a linear function of the height of the focal pixel. We tested 76 different combinations of the intercept and slope parameters of this linear function (Supplemental Data S1). For each of these parameter sets, we also tested three different CHM smoothing options. These smoothing functions were implemented as moving window algorithms which, for each pixel, computed the mean of all pixels in a $n$ x $n$ pixel square centered around the focal pixel and assigned the resulting value to the focal pixel. We tested a 5 x 5 pixel window (Smooth: 1), a 9 x 9 pixel window (Smooth: 2), and no smooth (Smooth 0). The smooths were applied prior to running the VWF algorithm. We included these smoothing options with the thought that they may smooth over 3D reconstruction artifacts of the photogrammetry algorithm. Factorially combining the three smooth options with each of the 76 variable window filter parameter sets resulted in testing 228 implementations of the VWF-based tree detection algorithm (Supplemental Data S1).

We additionally tested six algorithms designed to identify trees directly from 3D point clouds, implemented in the R packages lidR v3.0.4 (Roussel, 2021a) and lidRplugins v0.2.0 (Roussel, 2021b) (Supplemental Data S2). Most of these algorithms accept one or more parameters; we tested a variety of parameter combinations, focusing on those that Koontz et al. (2021) found to produce the best tree detection results. Two of the algorithms ('hamraz' and 'layerstacking'; Supplemental Data S2) were not tested by Koontz et al. The 'hamraz' algorithm requires no parameters and 'layerstacking' requires a single binary parameter for "hardwood" or "conifer"; we tested both. Additionally, for each point cloud-based algorithm, we tested the effect of thinning (“decimating”) the point cloud to 50 or 10 points m$^{-2}$ prior to running each algorithm. The multiple parameter combinations tested across all the point cloud-based tree detection methods resulted in a total of 58 methods tested. Combined with the CHM-based VWF methods, we tested a total of 286 tree detection methods for each Metashape photogrammetry workflow that was run for the Stage 1 comparisons (Table 4). For the Stage 2 comparisons, we used four top-performing tree detection methods (see *ITD performance evaluation*).

### *ITD performance evaluation*

We quantified the accuracy of the drone-derived tree maps by comparing each one against the 3.23-ha ground-based stem map. An initial coarse filter was applied to eliminate the very poor quality drone-derived maps: if the number of drone-mapped trees > 10 m height was more than 5 times the number of ground-mapped trees > 10 m height, or it it was less than 1/10 the number of ground-mapped trees > 10 m height, it was eliminated from the pool of candidates.

For all remaining drone-derived maps, we performed a comparison to the ground-derived map on a tree-by-tree basis, determining whether each ground-mapped tree was present in the drone-based map (true positives) and whether there were any additional trees in the drone-derived map that were not present in the ground-derived map (false positives). This required determining which tree (if any) from the ground-based map corresponded to which tree in the drone-based map (and vice-versa), a challenging and subjective exercise given that we never expect trees in a ground-based map to perfectly coincide with those in a drone-based map. Differences can arise duo to spatial errors in both mapping techniques and also due to the fact that the tree top (the point identified in the drone-based map) is often not located precisely above the stem (the point identified in the ground-based map).

For a drone-mapped tree to match with a ground-mapped tree, it was required to be within a distance ($d_{max}$) of the ground-mapped tree defined as a function of the height ($h$) of the ground-mapped tree as

$$d_{max} = 0.1h + 1,$$

where units are in meters. Its height was also required to be within ±50% of the height of the ground-mapped tree. Thus, for a ground-mapped tree 10 m tall, a drone-mapped tree needed to be within 2 m distance and its height needed to be between 5 and 15 m to match. For a ground-mapped tree 30 m tall, a drone-mapped tree needed to be within 4 m distance and its height between 15 and 45 m. Our distance matching threshold was generally similar to or more conservative than that used by previous studies (e.g., < 4 m used by Swayze et al., 2021 and < 3 m used by Creasy et al., 2021). We used a more liberal height range for tree mapping than previous studies (e.g., ±10% used by Creasy et al., 2021 and ±2 m used by Swayze et al., 2021) because (a) we wanted to avoid artificially reducing the estimated error in drone-based tree height measurement (as error estimation relies on comparing heights of drone-detected trees vs. paired ground-mapped trees) and (b) error in drone- vs. ground-mapped height substantially less than the matching threshold would provide confidence that trees were matched appropriately.

For each ground tree, the nearest matching drone tree was assigned as its match. If the same drone tree was assigned to multiple ground trees, it was removed from all of the ground trees except the one spatially closest to it. This procedure was repeated two more times, each time for the ground and drone trees remaining (unmatched) following the previous iteration. After the third iteration, no further matches were possible.

To quantify individual-tree detection (ITD) accuracy, we computed the true-positive rate (“sensitivity” or “recall”, the proportion of ground-mapped trees that had a matching drone-mapped tree) and the precision (the proportion of drone-mapped trees that matched a ground-mapped tree). Because it is possible for a tree detection algorithm to achieve high sensitivity at the expense of precision (and vice-versa), we also computed the F score, a statistic that integrates sensitivity and precision by computing their harmonic mean, thus disproportionately penalizing low values and favoring balanced sensitivity and precision. We computed sensitivity, precision, and F score two different tree size groups: trees ≥ 10 m height, and trees ≥ 20 m height.

There is potential for edge effects to confound the tree detection accuracy inferred via tree matching. If a ground-mapped tree were just inside the analysis boundary and the corresponding drone-mapped tree just outside it, the ground-mapped tree would be considered to not have a match (and thus constitute a false-negative detection). To minimize this effect, when calculating the proportion of drone-mapped trees that matched ground-mapped trees, we considered only drone-mapped trees that were at least 5 m inside the project boundary (so that they all had an opportunity to be matched with ground-mapped trees in any direction). We did the same with ground-mapped trees when calculating the proportion of ground-mapped trees that matched drone-mapped trees.

While it is valuable to know the proportion of all ground-truth trees that can be detected from aerial imagery, it is unrealistic to expect all trees to be detected, particularly in structurally complex stands like ours where small trees may be hidden under large trees or two immediately adjacent trees of similar size appear as one. Therefore, in addition to evaluating ITD performance across all trees, we evaluated performance in mapping “dominant” trees that did not have any immediately adjacent taller neighbors. We defined a ground-mapped tree as “dominant” if there was not a taller tree within a distance $d_{max}$, defined as a function of the difference in height between the two trees $\Delta h$ as

$$d_{max} = 0.1 * \Delta h + 1,$$

where units are in meters (Fig. S1). Thus, for example, a 20 m tall focal tree with a 30 m tall neighbor would be considered “dominant” if the neighbor were at least 2 m away. We consider this to be a conservative representation of the distance necessary for two trees to be distinct in aerial imagery (i.e., in many cases, a shorter tree more than $d_{max}$ meters away from its neighbors may still be obscured). For each drone-based tree map, we computed an additional set of ITD accuracy metrics assuming the only trees present in the ground-based map were “dominant” trees. This second set of metrics provides an assessment of the accuracy of the drone-based methods for mapping trees that are potentially aerially differentiable. Given the challenges of detecting trees hidden under the canopies of other trees, some ITD approaches have focused on mapping “tree-approximate objects” (TAOs; e.g., a tall tree with several shorter trees under it; Jeronimo et al., 2018), and our classification of “dominant” trees may approximate classification of TAOs.

*Identification of best-performing methods*

To identify the best performing photogrammetry and tree-detection parameter sets (Stage 1), we first determined, for each factorial combination of photo set (High nadir 90/90, Low nadir 90/90; Table 3), photogrammetry parameter set (1-12; Table 4), tree height class (> 10 m or > 20 m), and tree position class (all trees or dominant trees only), the tree detection algorithm that yielded the greatest F score. Using only those tree detection algorithms, we identified the photogrammetry parameter sets that most consistently yielded the highest, or near-highest, F scores across all factorial combinations of flight altitude, tree height class, and tree position class (Supplemental data S3). We selected four photogrammetry parameter sets. Using only those four sets, we then selected the tree detection parameter sets that most consistently yielded the highest, or near-highest, F scores across different factorial combinations of photogrammetry parameter set, flight altitude, tree height class, and tree position class (Supplemental data S4). We selected 8 tree detection parameter sets.

To quantify the influence of flight altitude, image overlap, and camera pitch on ITD performance (Stage 2), we used the four best-performing photogrammetry parameter sets, combined factorially with the eight best-performing tree detection methods, to produce 32 tree maps from each of the 22 different photo sets (Table 3). When plotting or describing tree detection performance achieved with any of these photo sets, we report the F score obtained from the tree detection method that produced the maximum F score for that photoset.

*Evaluation of drone-based tree height measurement*

To evaluate the potential to measure tree heights using drone imagery, we extracted tree heights from the canopy height model produced by using photogrammetry parameter set 16 on the high (120 m) nadir photo set with 90% front and side image overlap. We extracted the height value from the CHM pixel beneath each detected tree. We then compared these extracted heights to the ground-measured heights of the ground-truth trees to which the drone-detected trees were paired (see *ITD performance evaluation*). Ground-truth trees that were not paired with drone-detected trees, and vice versa, were not included in the comparison.

## Results

*Stage 1: Optimal photogrammetry and tree detection parameters*

Photogrammetry parameter combination 16 (medium alignment quality, high dense cloud quality, moderate depth filtering) consistently enabled the most accurate tree detection performance as quantified by F score (Fig. 2 and Supplemental Data S3), though the differences among parameter combinations were relatively small ($\Delta F < 0.04$). Medium alignment quality and high dense cloud quality both involve upscaling (coarsening) the image by a factor of 2 in both dimensions prior to running the algorithm. Parameter set 16 achieved the highest (or within 0.005 of the highest) F scores across all factorial combinations of flight altitude (90 m or

120 m), tree position (all trees or dominant trees), and tree height class (> 10 m or > 20 m). Therefore, for further evaluation, we focused on parameter set 16, along with parameter sets 9, 11, and 15, which were among the best-performing parameter sets for multiple combinations of tree height, tree position, and flight altitude (Supplemental Data S5). We thus selected a total of four photogrammetry parameter sets for further evaluation.

The most accurate tree detection methods, as quantified by F score, were all CHM-based VWF methods (Supplemental Data S4). This was true across all factorial combinations of flight altitude (90 m or 120 m), tree height class (> 10 m or > 20 m), tree position (all trees or dominant trees), and photogrammetry parameters (sets 9, 11, 15, and 16). Across all of these combinations, methods vwf_121 and vwf_196 most consistently achieved the highest (or within 0.005 of the highest) F scores for tree detection accuracy (Supplemental Data S4). Therefore, for further evaluation, we focused on these methods, along with six other consistently top-performing methods, vwf_109, vwf_110, vwf_113, vwf_120, vwf_122, vwf_185, for a total of 8 tree detection methods.

For a given scenario (e.g., flight altitude, tree position, tree height, camera pitch, and photo overlap), the F score achieved by the combination of photogrammetry parameter set 16 and tree detection method vwf_196 was generally within 0.01 of the maximum F score achieved by the optimal combination of photogrammetry parameter set (out of the four best-performing options) and tree detection method (out of the eight best-performing options) (e.g., Table 5). The difference in F score was less than 0.01 in approximately 80% of scenarios, particularly those with at least 90% front and side photo overlap and nadir images (Supplemental Data S5). In photo sets with less overlap and/or oblique images, other photogrammetry and tree detection parameters often performed better (F score difference > 0.01), but for these scenarios, even the optimal photogrammetry and tree detection parameter combinations yielded inferior tree mapping performance relative to higher overlap and/or nadir imagery (see next section).

For nadir photo sets with at least 90% front and side overlap, the optimal combination of photogrammetry and tree detection parameters achieved tree mapping accuracy ranging between F =  0.67 and F = 0.87 (Supplemental Data S5). For example, for dominant trees > 10 m tall, the optimal methods (photogrammetry parameter set 16 paired with tree detection method vwf_196) achieved an F score of 0.78, with a sensitivity of 0.69 and a precision of 0.90 (Table 5). Generally, precision was greater than sensitivity (Table 5 and Supplemental Data S5).

**Table 5:** Tree mapping accuracy achieved with the optimal combination of photogrammetry parameter set and tree detection method (Category 1) or with the specific combination of photogrammetry parameter set 16 and tree detection method vwf_196 (Category 2) for each factorial combination of tree position (dominant or all) and tree height class (> 20 m or > 10 m). All scenarios use the high (120 m altitude) nadir photo set with 90% front and side overlap. For two scenarios (dominant trees > 10 m and all trees > 20 m), the combination of photogrammetry parameter set 16 and tree detection method vwf_196 is the optimal combination. For accuracy metrics for different flight altitudes, camera pitches, and photo overlaps, see Supplemental Data S5.

| | | **Category 1: Photogrammetry and tree detection parameter sets yielding maximum F** | | | | | **Category 2: Photogrammetry parameter set 16 and tree detection method vwf_196** | | |
|---|---|---|---|---|---|---|---|---|---|
| **Canopy position** | **Tree height** | **Photogrammetry parameter set** | **Tree detection method** | **F score** | **Sensitivity** | **Precision** | **F score** | **Sensitivity** | **Precision** |
| dominant | > 20 m | 11 | vwf_122 | 0.865 | 0.838 | 0.894 | 0.864 | 0.841 | 0.887 |
| dominant | > 10 m | 16 | vwf_196 | 0.783 | 0.691 | 0.903 | 0.783 | 0.691 | 0.903 |
| all | > 20 m | 16 | vwf_196 | 0.826 | 0.756 | 0.909 | 0.826 | 0.756 | 0.909 |
| all | > 10 m | 15 | vwf_121 | 0.672 | 0.571 | 0.814 | 0.665 | 0.519 | 0.924 |

(a) All trees > 10 m

(b) All trees > 20 m

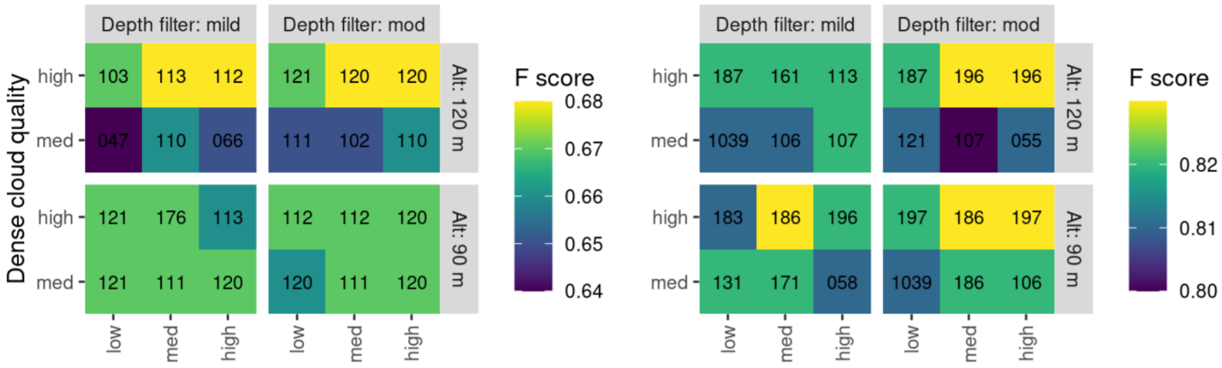

(c) Dominant trees > 10 m

(d) Dominant trees > 20 m

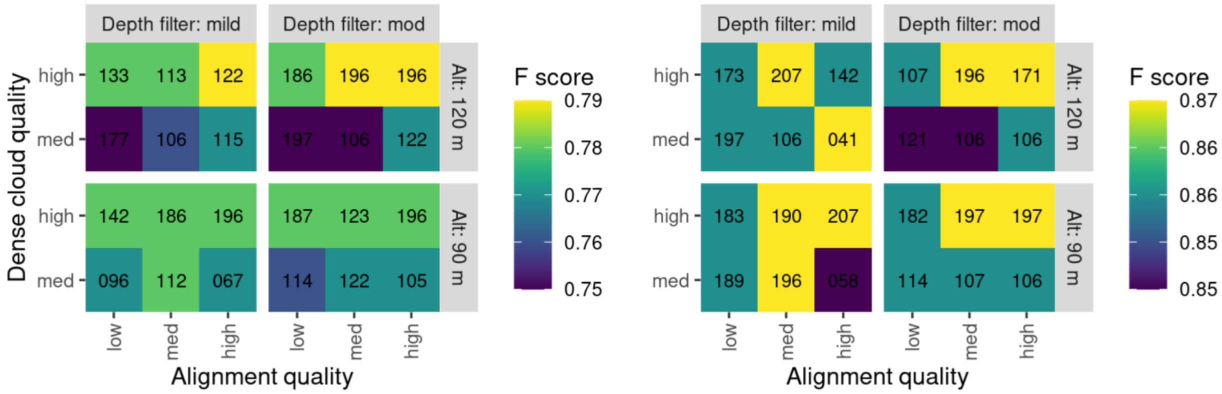

**Fig. 2:** Individual tree detection performance of different photogrammetry parameter combinations at two flight altitudes, for all trees (a, b) and dominant trees (c,d) with height > 10 m (a, c) or height > 20 m (b, d). The number in each cell indicates the ID of the tree detection method (Supplemental Data S1-S2) that yielded the maximum F score for the particular combination of parameters; 3-digit numbers refer to VWF methods, while 4-digit numbers refer to point cloud-based methods. The F score itself is indicated by the color. The aerial photo sets processed were the high nadir (Alt: 120 m) set and the low nadir (Alt: 90 m) set (both with 90% front and side image overlap) (bolded entries in Table 3).

### *Stage 2: Optimal image collection parameters*

Tree mapping accuracy tended to increase with increasing image overlap, to a point: once overlap reached 90%/80% (front/side), additional increase in overlap (to 90%/90% or greater) yielded little increase in accuracy (Fig. 3). At 90%/90% overlap, both 120 m and 90 m nadir flights yielded F scores of about 0.78 for dominant trees > 10 m tall and about 0.86 for dominant trees > 20 m tall (Table 5). Among nadir image sets, higher-altitude (120 m) sets tended to yield greater accuracy than lower-altitude sets when image overlaps were lower (below 90%/90%) and similar accuracy when overlaps were greater (90%/90% and greater) (Fig. 3). Interestingly, even though the 90%/80% and 80%/90% overlap image sets contained roughly the same image density, the former consistently enabled substantially greater tree mapping accuracy, for both 120 m and 90 m flights (Fig. 3).

Nadir imagery tended to achieve accuracy greater than or comparable to that of oblique or nadir-oblique composite imagery. The 120 m composite camera pitch image set performed as well as (at 95% front and side overlap) or substantially better than (at 90% front and side overlap) the 90 m composite pitch image set. For a similar image density (i.e., number of images), a 120 m nadir flight (at, e.g., 90%/80% overlap) yielded similar accuracy as the oblique flights (at, e.g., 85%/85% nominal overlap).

All of the results discussed thus far in this section assume that a given image set is processed using the photogrammetry and tree detection parameters that yield the greatest accuracy for that set. When using a single top-performing photogrammetry parameter set (16) combined with a single top-performing tree detection method (vwf_196), the patterns remain qualitatively very similar, with generally only very small shifts in tree detection accuracy (Fig. S2).

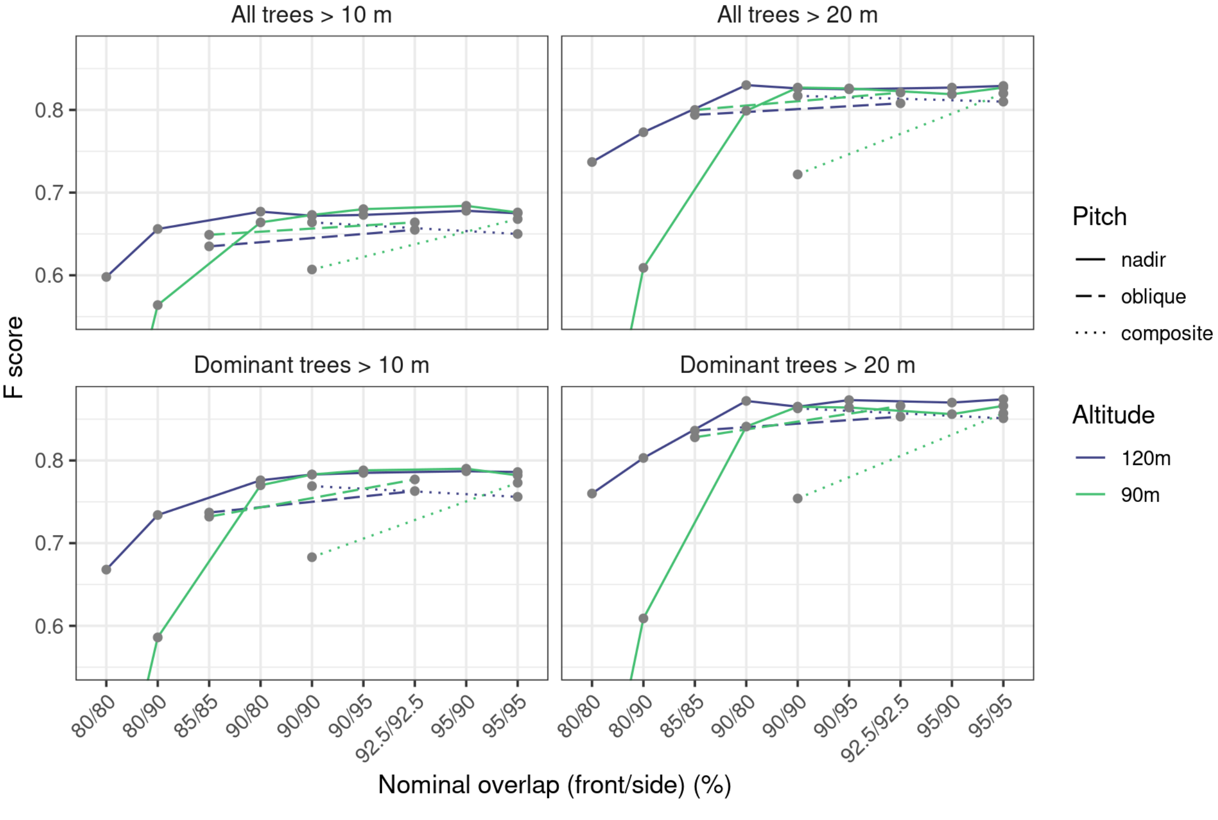

**Fig. 3:** Individual tree detection F score for different flight altitude, camera pitch, and image overlap combinations. For each combination, 8 top-performing tree detection methods were combined factorially with 4 top-performing photogrammetry processing parameter sets (see *Table 1: Stage 2*), and the F score depicted is the maximum across these 32 factorial combinations. For a version of this figure that uses only the single consistently best-performing tree detection method (vwf_196) combined with the best-performing photogrammetry parameter set (16), see Fig. S2.

*Tree height measurement*

Tree height measurement was generally highly accurate, with drone-measured and ground-measured tree heights corresponding with $R^2 = 0.95$, a mean bias of -0.86 m (with drone-derived heights generally shorter than their ground-truth counterparts), and a mean absolute error of 1.82 m (Fig. 4). The mean absolute error as a percentage of each tree's height was 9% and the mean bias was -3%.

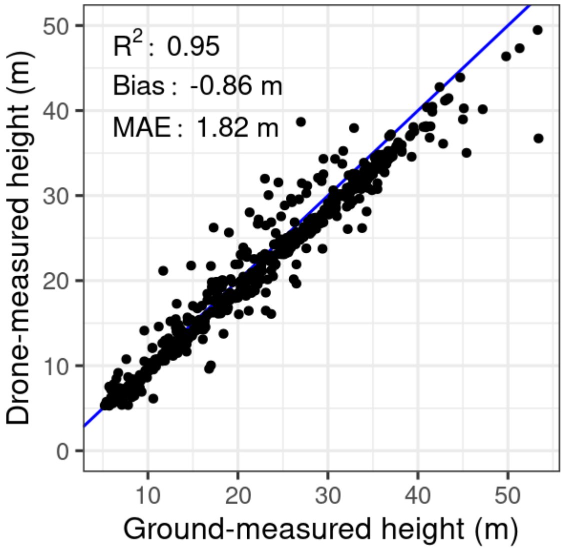

**Fig. 4:** Drone-based tree height measurements (height value of the CHM at each treetop location) relative to ground-truth tree heights for the most consistently best-performing tree detection method (vwf_196) applied to the CHM produced using the most consistently best-performing photogrammetry parameter combination (16) on the high (120 m) nadir 90% front and side overlap photo set.

## Discussion

### *Imagery acquisition and processing*

Our work helps to identify top-performing approaches to imagery collection and processing for SfM-based forest mapping in structurally complex conifer forests. Several clear and consistent results can help forest scientists and managers efficiently produce high-quality forest maps. First, a high (120 m) flight altitude consistently yielded tree maps with accuracy better than or effectively equivalent to those obtained from lower (90 m) flights (Fig. 3), consistent with previous observations that flight altitude has minimal impact (Swayze et al., 2021; Torres-Sánchez et al., 2018). Even in contexts where stem map quality is insensitive to flight altitude (in our case, when image overlap is 90% or greater), 120 m flights will likely be preferred given that they require fewer images to cover a landscape (as each image encompasses more ground area) and therefore less flight time.

Similarly, our work reveals little if any gain in ITD accuracy by increasing image overlap above 90% (front and side) (Fig. 3), consistent with previous results showing decreasing marginal returns to ITD accuracy with increasingly high overlap (Torres-Sánchez et al., 2018). In fact, given that increasing image overlap can substantially increase flight time (e.g., increasing side overlap from 90% to 95% doubles the number of transects, thus doubling flight time), flights with overlap > 90% may be undesirable. Reducing side overlap to 80% (while keeping front overlap at 90%) resulted in only minimal change in ITD accuracy. Therefore, given flight time constraints or the need to cover extensive area, 90%/80% front/side overlap may be preferable. Surprisingly, photo sets with 90%/80% front/side overlap consistently yielded ITD accuracy substantially greater than that from sets with 80%/90% front/side overlap (Fig. 3), despite the fact that the image density of these two sets is nominally identical. We speculate that high front overlap is more important for photogrammetry quality due to the aspect ratio of the photos (3:2 width:height). It may be more difficult for the photogrammetry algorithm to match and align photos along their short axis because that axis on average has fewer features (“keypoints”) to match; therefore, increasing the number of times a given feature appears along that axis by increasing the forward overlap may be disproportionately beneficial. Relatedly, optimal overlap may depend on image resolution (Ni et al., 2018), a relationship not tested in the present study.

We note that our approach to testing the effect of image overlap was somewhat artificial: rather than flying different missions with different overlaps, we flew a high-overlap (95% front and side) mission and progressively thinned the photos from it to produce the lower-overlap photo sets (*sensu* Frey et al., 2018; Ni et al., 2018; Torres-Sánchez et al., 2018). Because the flight speed of imaging drones performing SfM missions is generally limited by the speed of saving image files to the storage medium, our lower-overlap photo sets were collected with a slower flight speed than would likely be used for a mission designed to yield a lower overlap. This may mean that motion blur (the amount of ground distance passing during the time the shutter is open) may be artificially low for our photo sets. However, we expect this is unlikely to affect our inferences given that (a) motion blur of missions conducted at 90% overlap under the same lighting conditions do not exceed the camera’s ground sampling distance using automatic exposure settings (data not shown), (b) there was substantial room to increase shutter speed (and increase aperture to compensate) beyond the settings selected by the automatic exposure algorithm, and therefore future missions flown at a high speed could achieve lower motion blur with a similarly exposed photo, and (c) the optimal photogrammetry parameters involved upscaling (coarsening) the images by a factor of 2 in both dimensions, so even motion blur exceeding a single pixel’s ground sampling distance (but not exceeding two pixels’ ground sampling distance) should not affect photogrammetric processing.

Our tests of camera pitch revealed that oblique (25°) and oblique-nadir composite imagery, regardless of flight altitude, yielded ITD accuracy worse than nadir imagery collected at 120 m. This finding is surprising because oblique imagery is known to yield more accurate terrain models (Nesbit & Hugenholtz, 2019) and increase understory point cloud density (Díaz et al., 2020), but it corroborates existing evidence that for ITD specifically, greater accuracy is achieved with nadir imagery (Swayze et al., 2021). Although the improved understory imaging that is achieved by using oblique imagery can improve estimates of tree DBH (by enabling more accurate 3D modeling of tree stems; Swayze et al., 2021), it apparently does not improve the potential for detection of understory trees. This limitation to improvement may be explained by the fact that all CHM-based tree detection algorithms and many point cloud-based tree detection algorithms (e.g., Li et al., 2012) are not designed to detect one tree beneath another, so improved imaging of the understory cannot translate to improved tree detection. Improvements multi-layer tree detection algorithms (e.g., Torresan et al., 2020; Xiao et al., 2019), and implementations of them in common point cloud processing platforms (e.g., the R package lidR; Roussel, 2021a), may make understory imaging (and thus oblique camera angles) more valuable for ITD in the future.

We expect our results are applicable to many widely used, relatively low cost drones with camera resolution and field of view similar to ours. In fact, given that all image processing steps utilize images that have been upscaled (coarsened) 2-fold in both dimensions (thus converting a 20 megapixel image to 5 megapixels), the same dataset could in theory be generated with a 5 megapixel camera by eliminating the upscaling step. Similarly, imagery from a higher-resolution camera could be used optimally by increasing the upscaling factor. While this may represent a waste of data, the coarser scale may actually achieve greater mapping accuracy given that tree canopies largely consist of small surfaces (e.g., leaves, branches) that are susceptible to moving in the wind and thus confounding the image-matching algorithms at the heart of photogrammetry software.

### *Tree detection algorithms*

Despite testing 6 point cloud-based ITD algorithms (and 58 different parameterizations of them), focusing on the algorithms and parameterizations that yielded the best performance for Koontz et al. (2021), the CHM-based VWF algorithm consistently performed the best (Supplemental Data S4). While variations of the VWF method have performed well for other SfM-based ITD work (Creasy et al., 2021; Mohan et al., 2017; Swayze et al., 2021), the method was not a top performer in the comparison performed by Koontz et al. (2021). The disagreement on top-performing algorithm may be explained by several differences in methodology. First, we tested 228 parameterizations of the VWF method (or 76 if the 3 initial CHM smoothing alternatives are not considered parameterizations), whereas Koontz et al. (2021) tested 3, limiting the likelihood that one would be a top-performing method. Second, before performing tree detection, we first smoothed the CHM using a moving-window mean with a 5x5 or 9x9 pixel window, whereas Koontz et al. (2021) used a 3x3 window. Finally, the photogrammetry algorithm used by Koontz et al. (2021), implemented using Pix4Dmapper Cloud (Pix4D SA), appeared to yield digital surface models, and thus CHMs, that capture more fine-scale heterogeneity in the canopies of individual trees (datasets accompanying Koontz et al., 2021), potentially confounding the VWF algorithm, particularly given the CHMs were smoothed with a relatively small moving window.

Despite the strong performance of CHM-based ITD algorithms in our analysis, CHM-based methods have the inherent limitation that a CHM, which takes the form of a 2D raster, cannot capture multiple strata of trees (i.e., one tree under another) even if they were detected by the sensor and represented as distinct point clouds by the photogrammetry algorithm; a CHM only provides the elevation of the tallest surface at each x,y location.

Multi-stratum tree mapping will thus rely on applying ITD algorithms to point clouds, polygonal models, or other representations of 3D structure. Improvements to current point cloud-based algorithms that can detect multiple strata (e.g., Torresan et al., 2020; Xiao et al., 2019) should enable improved mapping of understory trees, and with accurate multi-stratum ITD algorithms, oblique imagery may become more important (see Discussion section *Imagery acquisition*).

As with other SfM-based work (e.g., Creasy et al., 2021; Tinkham & Swayze, 2021) and LiDAR-based work (Ferraz et al., 2012; Jeronimo et al., 2018), we observed substantially improved ITD performance for taller trees and canopy-dominant trees (e.g., F = 0.78 for canopy-dominant trees > 10 m height vs. F = 0.67 for all trees > 10 m height). This pattern makes sense considering structure can only be mapped for surfaces that are detected by the sensor (which are disproportionately the top-of-canopy objects, especially for SfM; (Jayathunga et al., 2018; Lisein et al., 2013). Even when using LiDAR, which usually can penetrate the canopy to some extent, understory and mid-story detail, and thus potential to detect trees there, is limited (Richardson & Moskal, 2011) and has led some to re-focus detection and mapping of individual trees (ITD) toward detection and mapping of tree-approximate objects (TAOs), which can include single trees and clusters of trees that are not differentiable (Jeronimo et al., 2018; North et al., 2017). Maps of the size and arrangement of TAOs may be valuable for some management applications (Jeronimo et al., 2018; North et al., 2017), and important ecological questions can be addressed using maps of the specific trees visible from above (Brandt et al., 2020; Weinstein et al., 2021) or detectable using SfM that is not canopy-penetrating (Koontz et al., 2021). Our calculation of ITD accuracy metrics specifically for “overstory” trees helps to provide a sense of TAO mapping accuracy. Given we used a conservative set of parameters for classifying a tree as “canopy dominant” (Fig. S1), our accuracy metrics may be underestimates.

Notably, our ITD precision values were consistently higher than the sensitivity values, especially for all trees (as opposed to canopy-dominant trees) (Table 5 and Supplemental Data S5), indicating that the ITD algorithm failed to detect some trees at the expense of minimizing false-positives. This suggests that there is some potential to select an ITD parameterization with greater tree detection sensitivity. This may increase the false-positive rate (resulting in an overall lower F score), but future work may incorporate an additional “detected tree screening” stage that uses information besides the CHM or point cloud to identify and reject false positives. For example, Bonnet et al. (2017) used a machine learning approach to predict tree detections as true or false positives based on the textural and spectral characteristics of the detected objects and thereby reduced the false-positive rate from 75-82% to 3-8%. Incorporating both structural and spectral data (e.g., taking advantage of the fact that points in SfM-derived point clouds, in contrast to LiDAR-derived clouds, can be assigned spectral values) in tree detection algorithms may improve tree detection sensitivity (Yancho et al., 2019).

### *Tree height measurement and matching of ground and drone trees*

The canopy height model resulting from the optimal photogrammetry parameter set provided a relatively accurate representation of tree heights (Fig. 4). The small negative height bias (CHM heights < field-measured heights) generally increased with increasing tree height, suggesting either (a) disproportionate overestimation of tall tree heights during ground surveys or (b) disproportionate underestimation of tall tree heights by the photogrammetry algorithm.

Given that CHM generation involves some degree of interpolation and smoothing of the point cloud, it may make sense that objects that are disproportionately tall relative to their surroundings are underestimated by the CHM. Nonetheless, the mean absolute height error was relatively small (1.8 m or 9% of tree height). Further, given that our algorithm for matching SfM-detected trees with ground-measured trees required the SfM tree to be within ± 50% of the height of the ground tree, the fact that the mean height difference was only 9% strongly suggests that trees were generally matched correctly. Our SfM-based tree height measurement accuracy was generally comparable to or better than other SfM-based approaches, which have obtained $R^2 = 0.71$ (Belmonte et al., 2020), RMSE = 9-15% (Creasy et al., 2021), RMSE = 24% (Tinkham & Swayze, 2021), and $R^2 = 0.99$ and RMSE = 18% (Swayze et al., 2021).

*Integrative assessment and conclusions*

Potentially due to the comprehensive evaluation of numerous SfM imagery collection, imagery processing, and tree detection methods, the ITD performance we achieved meets or exceeds expectations based on previous work. With relatively high image overlap (> 90% front and side), Swayze et al. (2021) obtained a maximum F score of 0.77 for all trees, and Tinkham and Swayze (2021) obtained a maximum F score of 0.72 for overstory trees. The work by Tinkham and Swayze (2021) and Swayze et al. (2021) was conducted in a relatively low-density forest (trees > 5 m height: 374 ha$^{-1}$ relative to our 551 ha$^{-1}$) with low structural complexity (generally two distinct size classes that are spatially clustered rather than interspersed with layered strata) and a single dominant conifer species, so the F scores we obtained (0.67-0.86 depending on canopy position and height; Table 5) suggest strong performance. The ITD performance we achieved appears improved relative to that observed by Koontz et al. (2021) in Sierra Nevada forests of similar or lower density, where RMSE of tree count ranged between 46% and 75% of ground-mapped tree count. Our understory (F score: 0.67) and overstory (F score: 0.78-0.87) ITD accuracy was also greater than that obtained by Creasy et al. (2021) (F score: 0.51-0.57 for understory and intermediate trees and F score: 0.75 for overstory trees). The stands studied by Creasy et al. (2021) had much greater reported density (1379-1537 trees ha$^{-1}$ for trees > 6-8 m height), though these reported density values may be misreported given the forest type (nearly monodominant ponderosa pine) and given that a different study at one of the same sites (Swayze et al. 2021) reported density of trees > 5 m height to be 374 trees ha$^{-1}$. In an Arizona ponderosa pine forest, Belmonte et al. (2020) detected trees in low-density stands (mean density: 59 trees ha$^{-1}$) with F = 0.94, in moderate-density stands (mean density: 139 trees ha$^{-1}$) with F = 0.8, and in high-density stands (mean density: 778 trees ha$^{-1}$) with F = 0.44.

Given the potential for LiDAR data to enable better understory modeling, one may ask whether ITD performance would be improved by using LiDAR data relative to SfM applied to aerial images. ITD methods applied to airborne LiDAR data (e.g., Ferraz et al., 2012; Jeronimo et al., 2018; Silva et al., 2016; Zaforemska et al., 2019) show a wide range of accuracies, likely due to variation in LiDAR point density, stand density, and tree detection method, making comparison among methods difficult. Applying ITD to LiDAR data with mean point density of 9-12 pulses m$^{-2}$ acquired from mixed-conifer stands in the central Sierra Nevada with tree density averaging 391 trees ha$^{-1}$, Jeronimo et al. (2018) obtained an ITD F score of 0.50 for trees with DBH > 25 cm. Higher LiDAR point density, such as that sometimes associated with drone-based LiDAR acquisitions, can enable much more accurate ITD (Zaforemska et al., 2019), though the associated costs may be prohibitive in many contexts.

The majority of SfM-based ITD work to date has been conducted in relatively low density monodominant stands with low structural complexity. Our work demonstrates that SfM-based ITD can also be a practical approach to tree mapping in denser, more structurally complex stands, especially if the focus is on canopy-dominant trees or TAOs. To evaluate the extent to which the ITD accuracy and optimal parameter sets we identified may extend to other forest stands, perhaps the most important considerations are stand density and structural complexity (Jeronimo et al., 2018). In forests with lower tree density and limited multi-stratum structure, such as many ponderosa pine-dominated forests of the southwestern U.S. (e.g., Swayze et al. 2021), we might expect higher accuracy than we achieved; we might expect the reverse for denser or more structurally complex stands. Historical densities of trees > 10 cm DBH in the yellow pine and mixed-conifer forests of California's Sierra Nevada averaged roughly 195 trees ha$^{-1}$ (Safford & Stevens, 2017; Young et al., 2020), relative to the 593 trees ha$^{-1}$ in our mixed-conifer stand. With contemporary stands roughly 2-4-fold denser than historically (Safford & Stevens, 2017) (therefore, roughly 400-800 trees ha$^{-1}$), our focal stand may be roughly reflective of mean contemporary California mixed-conifer forest structure and thus of expected ITD performance. In denser stands with strong multi-stratum structure, the use of oblique images, coupled with a point-cloud based ITD algorithm, will likely become more important for capturing understory trees (see Discussion section *Imagery acquisition*). With additional refinements (e.g., use of a more sensitive tree detection algorithm with a false-positive filtering step, improvement of point cloud-based multi-layer tree detection algorithms, and application of deep learning computer vision to tree detection; Weinstein, weinstein), the accuracy and applicability of drone-based forest mapping will continue to improve.

## Acknowledgments

Our Emerald Point study site is located in the homeland of the Washoe people. We thank data technicians H. de la Calle and S. Sundaram for their careful organization of the drone imagery, identification of ground control points, and preparation of the ground-truth stem map data. We thank A. Barker and R. Cuevas for assisting with ground-truth stem map data collection and D. Shaw for facilitating field logistics. We thank A. Latimer for assistance acquiring drone equipment and computing resources. We thank A. Mandel and other contributors to the reproducible photogrammetry workflow software library we used.

## Literature cited

Ager, A. A., Day, M. A., Waltz, A., Nigrelli, M., Volger, K. C., & Lata, M. (2021). Balancing ecological and economic objectives in restoration of fire-adapted forests: Case study from the Four Forest Restoration Initiative. *Gen. Tech. Rep. RMRS-GTR-424. Fort Collins, CO: U.S. Department of Agriculture, Forest Service, Rocky Mountain Research Station. 30 p. Https://Doi.Org/10.2737/RMRS-GTR-424.*, *424*. https://doi.org/10.2737/RMRS-GTR-424

Agisoft. (2020). *Metashape v1.6 downscale parameter*. https://www.agisoft.com/forum/index.php?topic=11697.0

Bazzaz, F. A. (1975). Plant Species Diversity in Old-Field Successional Ecosystems in Southern Illinois. *Ecology*, *56*(2), 485–488. https://doi.org/10.2307/1934981

Belmonte, A., Sankey, T., Biederman, J. A., Bradford, J., Goetz, S. J., Kolb, T., & Woolley, T. (2020). UAV-derived estimates of forest structure to inform ponderosa pine forest restoration. *Remote Sensing in Ecology and Conservation*, *6*(2), 181–197. https://doi.org/10.1002/rse2.137

Bonnet, S., Lisein, J., & Lejeune, P. (2017). Comparison of UAS photogrammetric products for tree detection and characterization of coniferous stands. *International Journal of Remote Sensing*, *38*(19), 5310–5337. https://doi.org/10.1080/01431161.2017.1338839

Brandt, M., Tucker, C. J., Kariryaa, A., Rasmussen, K., Abel, C., Small, J., Chave, J., Rasmussen, L. V., Hiernaux, P., Diouf, A. A., Kergoat, L., Mertz, O., Igel, C., Gieseke, F., Schöning, J., Li, S., Melocik, K., Meyer, J., Sinno, S., … Fensholt, R. (2020). An unexpectedly large count of trees in the West African Sahara and Sahel. *Nature*, 1–5. https://doi.org/10.1038/s41586-020-2824-5

Camarretta, N., Harrison, P. A., Bailey, T., Potts, B., Lucieer, A., Davidson, N., & Hunt, M. (2020). Monitoring forest structure to guide adaptive management of forest restoration: A review of remote sensing approaches. *New Forests*, *51*(4), 573–596. https://doi.org/10.1007/s11056-019-09754-5

Creasy, M. B., Tinkham, W. T., Hoffman, C. M., & Vogeler, J. C. (2021). Potential for Individual Tree Monitoring in Ponderosa Pine-Dominated Forests Using Unmanned Aerial System Structure from Motion Point Clouds. *Canadian Journal of Forest Research*, cjfr-2020-0433. https://doi.org/10.1139/cjfr-2020-0433

Dandois, J. P., & Ellis, E. C. (2013). High spatial resolution three-dimensional mapping of vegetation spectral dynamics using computer vision. *Remote Sensing of Environment*, *136*, 259–276. https://doi.org/10.1016/j.rse.2013.04.005

De Luca, G., N. Silva, J. M., Cerasoli, S., Araújo, J., Campos, J., Di Fazio, S., & Modica, G. (2019). Object-Based Land Cover Classification of Cork Oak Woodlands using UAV Imagery and Orfeo ToolBox. *Remote Sensing*, *11*(10), 1238. https://doi.org/10.3390/rs11101238

Díaz, G. M., Mohr-Bell, D., Garrett, M., Muñoz, L., & Lencinas, J. D. (2020). Customizing unmanned aircraft systems to reduce forest inventory costs: Can oblique images substantially improve the 3D reconstruction of the canopy? *International Journal of Remote Sensing*, *41*(9), 3480–3510. https://doi.org/10.1080/01431161.2019.1706200

Dixon, G. E. (2002). Essential FVS: A user's guide to the Forest Vegetation Simulator. *Internal Rep. Fort Collins, CO: US Department of Agriculture, Forest Service, Forest Management Service Center*, *193*.

Ferraz, A., Bretar, F., Jacquemoud, S., Gonçalves, G., Pereira, L., Tomé, M., & Soares, P. (2012). 3-D mapping of a multi-layered Mediterranean forest using ALS data. *Remote Sensing of Environment*, *121*, 210–223. https://doi.org/10.1016/j.rse.2012.01.020

Frey, J., Kovach, K., Stemmler, S., & Koch, B. (2018). UAV Photogrammetry of Forests as a

Vulnerable Process. A Sensitivity Analysis for a Structure from Motion RGB-Image Pipeline. *Remote Sensing*, *10*(6), 912. https://doi.org/10.3390/rs10060912

Gray, A. N., Brandeis, T. J., Shaw, J. D., McWilliams, W. H., & Miles, P. (2012). Forest Inventory and Analysis Database of the United States of America (FIA). *In: Dengler, J.; Oldeland, J.; Jansen, F.; Chytry, M.; Ewald, J., Finckh, M.; Glockler, F.; Lopez-Gonzalez, G.; Peet, R. K.; Schaminee, J .H. J., Eds. Vegetation Databases for the 21st Century. Biodiversity and Ecology. 4: 225-231.*, 225–231. https://doi.org/10.7809/b-e.00079

Hubbell, S. P., Foster, R. B., O'Brien, S. T., Harms, K. E., Condit, R., Wechsler, B., Wright, S. J., & Lao, S. L. de. (1999). Light-Gap Disturbances, Recruitment Limitation, and Tree Diversity in a Neotropical Forest. *Science*, *283*(5401), 554–557. https://doi.org/10.1126/science.283.5401.554

James, M. R., & Robson, S. (2014). Mitigating systematic error in topographic models derived from UAV and ground-based image networks. *Earth Surface Processes and Landforms*, *39*(10), 1413–1420. https://doi.org/10.1002/esp.3609

Jayathunga, S., Owari, T., & Tsuyuki, S. (2018). The use of fixed–wing UAV photogrammetry with LiDAR DTM to estimate merchantable volume and carbon stock in living biomass over a mixed conifer–broadleaf forest. *International Journal of Applied Earth Observation and Geoinformation*, *73*, 767–777. https://doi.org/10.1016/j.jag.2018.08.017

Jeronimo, S. M. A., Kane, V. R., Churchill, D. J., McGaughey, R. J., & Franklin, J. F. (2018). Applying LiDAR Individual Tree Detection to Management of Structurally Diverse Forest Landscapes. *Journal of Forestry*, *116*(4), 336–346. https://doi.org/10.1093/jofore/fvy023

Koontz, M. J., Latimer, A. M., Mortenson, L. A., Fettig, C. J., & North, M. P. (2021). Cross-scale interaction of host tree size and climatic water deficit governs bark beetle-induced tree mortality. *Nature Communications*, *12*(1), 129. https://doi.org/10.1038/s41467-020-20455-y

Lasky, J. R., Uriarte, M., Boukili, V. K., Erickson, D. L., Kress, W. J., & Chazdon, R. L. (2014). The relationship between tree biodiversity and biomass dynamics changes with tropical forest succession. *Ecology Letters*, *17*(9), 1158–1167. https://doi.org/10.1111/ele.12322

Li, W., Guo, Q., Jakubowski, M. K., & Kelly, M. (2012). A New Method for Segmenting Individual Trees from the Lidar Point Cloud. *Photogrammetric Engineering & Remote Sensing*, *78*(1), 75–84. https://doi.org/10.14358/PERS.78.1.75

Lisein, J., Pierrot-Deseilligny, M., Bonnet, S., & Lejeune, P. (2013). A Photogrammetric Workflow for the Creation of a Forest Canopy Height Model from Small Unmanned Aerial System Imagery. *Forests*, *4*(4), 922–944. https://doi.org/10.3390/f4040922

Mlambo, R., Woodhouse, I. H., Gerard, F., & Anderson, K. (2017). Structure from Motion (SfM) Photogrammetry with Drone Data: A Low Cost Method for Monitoring Greenhouse Gas Emissions from Forests in Developing Countries. *Forests*, *8*(3), 68. https://doi.org/10.3390/f8030068

Mohan, M., Silva, C., Klauberg, C., Jat, P., Catts, G., Cardil, A., Hudak, A., & Dia, M. (2017). Individual tree detection from unmanned aerial vehicle (UAV) derived canopy height model in an open canopy mixed conifer forest. *Forests*, *8*(9), 340. https://doi.org/10.3390/f8090340

Nesbit, P. R., & Hugenholtz, C. H. (2019). Enhancing UAV–SfM 3D Model Accuracy in High-Relief Landscapes by Incorporating Oblique Images. *Remote Sensing*, *11*(3), 239. https://doi.org/10.3390/rs11030239

Ni, W., Sun, G., Pang, Y., Zhang, Z., Liu, J., Yang, A., Wang, Y., & Zhang, D. (2018). Mapping Three-Dimensional Structures of Forest Canopy Using UAV Stereo Imagery: Evaluating Impacts of Forward Overlaps and Image Resolutions With LiDAR Data as Reference. *IEEE Journal of Selected Topics in Applied Earth Observations and Remote Sensing*, *11*(10), 3578–3589. https://doi.org/10.1109/JSTARS.2018.2867945

North, M. P., Kane, J. T., Kane, V. R., Asner, G. P., Berigan, W., Churchill, D. J., Conway, S., Gutiérrez, R. J., Jeronimo, S., Keane, J., Koltunov, A., Mark, T., Moskal, M., Munton, T., Peery, Z., Ramirez, C., Sollmann, R., White, A., & Whitmore, S. (2017). Cover of tall trees best predicts California spotted owl habitat. *Forest Ecology and Management*, *405*, 166–178. https://doi.org/10.1016/j.foreco.2017.09.019

North, M. P., York, R. A., Collins, B. M., Hurteau, M. D., Jones, G. M., Knapp, E. E., Kobziar, L., McCann, H., Meyer, M. D., Stephens, S. L., Tompkins, R. E., & Tubbesing, C. L. (2021). Pyrosilviculture Needed for Landscape Resilience of Dry Western United States Forests. *Journal of Forestry*, *119*(5), 520–544. https://doi.org/10.1093/jofore/fvab026

Plowright, A. (2021). *ForestTools: Analyzing Remotely Sensed Forest Data*. Comprehensive R Archive Network (CRAN). https://CRAN.R-project.org/package=ForestTools

Popescu, S. C., & Wynne, R. H. (2004). Seeing the Trees in the Forest. *Photogrammetric Engineering & Remote Sensing*, *70*(5), 589–604. https://doi.org/10.14358/PERS.70.5.589

Puliti, S., Solberg, S., & Granhus, A. (2019). Use of UAV photogrammetric data for estimation of biophysical properties in forest stands under regeneration. *Remote Sensing*, *11*(3), 233. https://doi.org/10.3390/rs11030233

R Core Team. (2020). *R version 3.6.3*. R: A language and environment for statistical computing. R Foundation for Statistical Computing, Vienna, Austria.

Richardson, J. J., & Moskal, L. M. (2011). Strengths and limitations of assessing forest density and spatial configuration with aerial LiDAR. *Remote Sensing of Environment*, *115*(10), 2640–2651. https://doi.org/10.1016/j.rse.2011.05.020

Rodman, K. C., Veblen, T. T., Saraceni, S., & Chapman, T. B. (2019). Wildfire activity and land use drove 20th-century changes in forest cover in the Colorado front range. *Ecosphere*, *10*(2), e02594. https://doi.org/10.1002/ecs2.2594

Roussel, J.-R. (2021a, May 20). *Airborne LiDAR Data Manipulation and Visualization for Forestry Applications [R package lidR version 3.0.4]*. Comprehensive R Archive Network (CRAN). https://CRAN.R-project.org/package=lidR

Roussel, J.-R. (2021b, May 20). *Extra functions and algorithms for lidR package [R package lidRplugins version 0.2.0]*. https://github.com/Jean-Romain/lidRplugins

Safford, H. D., & Stevens, J. T. (2017). Natural range of variation for yellow pine and mixed-conifer forests in the Sierra Nevada, southern Cascades, and Modoc and Inyo National Forests, California, USA. *Gen. Tech. Rep. PSW-GTR-256. Albany, CA: U.S. Department of Agriculture, Forest Service, Pacific Southwest Research Station. 229 p.*, *256*. https://www.fs.usda.gov/treesearch/pubs/55393

Shin, P., Sankey, T., Moore, M. M., & Thode, A. E. (2018). Evaluating Unmanned Aerial Vehicle Images for Estimating Forest Canopy Fuels in a Ponderosa Pine Stand. *Remote Sensing*, *10*(8), 1266. https://doi.org/10.3390/rs10081266

Silva, C. A., Hudak, A. T., Vierling, L. A., Loudermilk, E. L., O'Brien, J. J., Hiers, J. K., Jack, S. B., Gonzalez-Benecke, C., Lee, H., Falkowski, M. J., & Khosravipour, A. (2016). Imputation of Individual Longleaf Pine (Pinus palustris Mill.) Tree Attributes from Field and LiDAR Data. *Canadian Journal of Remote Sensing*, *42*(5), 554–573. https://doi.org/10.1080/07038992.2016.1196582

Swayze, N. C., Tinkham, W. T., Vogeler, J. C., & Hudak, A. T. (2021). Influence of flight parameters on UAS-based monitoring of tree height, diameter, and density. *Remote Sensing of Environment*, *263*, 112540. https://doi.org/10.1016/j.rse.2021.112540

Tinkham, W. T., & Swayze, N. C. (2021). Influence of Agisoft Metashape Parameters on UAS Structure from Motion Individual Tree Detection from Canopy Height Models. *Forests*, *12*(2), 250. https://doi.org/10.3390/f12020250

Torresan, C., Carotenuto, F., Chiavetta, U., Miglietta, F., Zaldei, A., & Gioli, B. (2020). Individual Tree Crown Segmentation in Two-Layered Dense Mixed Forests from UAV LiDAR Data. *Drones*, *4*(2), 10. https://doi.org/10.3390/drones4020010

Torres-Sánchez, J., López-Granados, F., Borra-Serrano, I., & Peña, J. M. (2018). Assessing UAV-collected image overlap influence on computation time and digital surface model accuracy in olive orchards. *Precision Agriculture*, *19*(1), 115–133. https://doi.org/10.1007/s11119-017-9502-0

USDA Forest Service. (2016). *Forest Inventory and Analysis Strategic Plan FS-1079*. https://www.fia.fs.fed.us/library/bus-org-documents/docs/strategic-plan-docs/FIA%20Strategic%20Plan%20FS-1079.pdf

USGS. (2017). *Unmanned Aircraft Systems Data Post-Processing: Structure-from-Motion Photogrammetry*. National Unmanned Aircraft Systems (UAS) Project Office. https://uas.usgs.gov/nupo/pdf/PhotoScanProcessingDSLRMar2017.pdf

USGS. (2018). *3DEP products and services: The National Map, 3D Elevation Program, https://nationalmap.gov/3DEP/*.

Weinstein, B. G., Marconi, S., Bohlman, S. A., Zare, A., Singh, A., Graves, S. J., & White, E. P. (2021). A remote sensing derived data set of 100 million individual tree crowns for the National Ecological Observatory Network. *ELife*, *10*, e62922. https://doi.org/10.7554/eLife.62922

Westoby, M. J., Brasington, J., Glasser, N. F., Hambrey, M. J., & Reynolds, J. M. (2012). 'Structure-from-Motion' photogrammetry: A low-cost, effective tool for geoscience applications. *Geomorphology*, *179*, 300–314. https://doi.org/10.1016/j.geomorph.2012.08.021

Whittaker, R. H. (1956). Vegetation of the Great Smoky Mountains. *Ecological Monographs*, *26*(1), 1–80. https://doi.org/10.2307/1943577

Wright, S. J., Kitajima, K., Kraft, N. J. B., Reich, P. B., Wright, I. J., Bunker, D. E., Condit, R., Dalling, J. W., Davies, S. J., Díaz, S., Engelbrecht, B. M. J., Harms, K. E., Hubbell, S. P., Marks, C. O., Ruiz-Jaen, M. C., Salvador, C. M., & Zanne, A. E. (2010). Functional traits and the growth–mortality trade-off in tropical trees. *Ecology*, *91*(12), 3664–3674. https://doi.org/10.1890/09-2335.1

Xiao, W., Zaforemska, A., Smigaj, M., Wang, Y., & Gaulton, R. (2019). Mean Shift Segmentation Assessment for Individual Forest Tree Delineation from Airborne Lidar Data. *Remote Sensing*, *11*(11), 1263. https://doi.org/10.3390/rs11111263

Yancho, J. M. M., Coops, N. C., Tompalski, P., Goodbody, T. R. H., & Plowright, A. (2019). Fine-Scale Spatial and Spectral Clustering of UAV-Acquired Digital Aerial Photogrammetric (DAP) Point Clouds for Individual Tree Crown Detection and Segmentation. *IEEE Journal of Selected Topics in Applied Earth Observations and Remote Sensing*, *12*(10), 4131–4148. https://doi.org/10.1109/JSTARS.2019.2942811

Young, D., Alex, Alexander, MallikaNocco, & Hereñú, D. (2021). *ucdavis/metashape: V0.1.0*. Zenodo. https://doi.org/10.5281/zenodo.5088962

Young, D., Meyer, M., Estes, B., Gross, S., Wuenschel, A., Restaino, C., & Safford, H. D. (2020). Forest recovery following extreme drought in California, USA: Natural patterns and effects of pre-drought management. *Ecological Applications*, *30*(1), e02002. https://doi.org/10.1002/eap.2002

Zaforemska, A., Xiao, W., & Gaulton, R. (2019). INDIVIDUAL TREE DETECTION FROM UAV LIDAR DATA IN A MIXED SPECIES WOODLAND. *ISPRS - International Archives of the Photogrammetry, Remote Sensing and Spatial Information Sciences*, *XLII-2/W13*, 657–663. https://doi.org/10.5194/isprs-archives-XLII-2-W13-657-2019